

Mode Conversion Trimming in Asymmetric Directional Couplers Enabled by Silicon Ion Implantation

Rongyang Xu,[†] Shabnam Taheriniya,[†] Akhil Varri, Mark Ulanov, Iurii Konyshev, Linus Krämer, Liam McRae, Falk Leonard Ebert, Julian Rasmus Bankwitz, Xinyu Ma, Simone Ferrari, Harish Bhaskaran, and Wolfram H. P. Pernice*



Cite This: <https://doi.org/10.1021/acs.nanolett.4c02065>



Read Online

ACCESS |

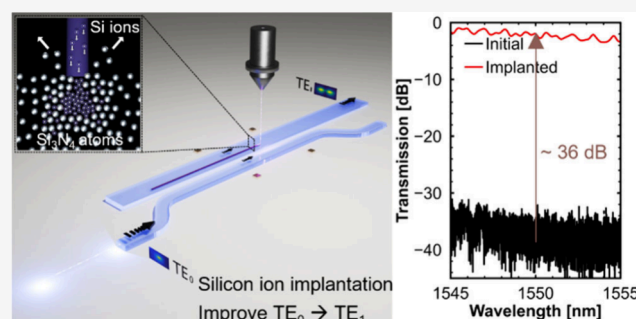
Metrics & More

Article Recommendations

Supporting Information

ABSTRACT: An on-chip asymmetric directional coupler (DC) can convert fundamental modes to higher-order modes and is one of the core components of mode-division multiplexing (MDM) technology. In this study, we propose that waveguides of the asymmetric DC can be trimmed by silicon ion implantation to tune the effective refractive index and facilitate mode conversion into higher-order modes. Through this method of tuning, transmission changes of up to 18 dB have been realized with one ion implantation step. In addition, adjusting the position of the ion implantation on the waveguide can provide a further degree of control over the transmission into the resulting mode. The results of this work present a promising new route for the development of high-efficiency, low-loss mode converters for integrated photonic platforms, and aim to facilitate the application of MDM technology in emerging photonic neuromorphic computing.

KEYWORDS: Photonic integrated circuits, mode conversion, asymmetric directional couplers, silicon ion implantation



Photonic integrated circuits (PIC), which are microchips integrating various photonic components, have great potential in application areas such as optical interconnects,^{1–3} quantum computing,^{4–9} and neuromorphic computing.^{10–18} By leveraging the inherent parallelism of light, multiplexing techniques in PICs have provided a promising route to realize high data throughput. Wavelength-division multiplexing (WDM) is a technique commonly used in PICs to significantly increase data rates.^{19,20} For instance, a relatively simple multimodulator setup can achieve a data bandwidth approaching 250 Gbps when operating at a speed of 25 Gbps.²¹ Moreover, utilizing WDM, PICs based on crossbar arrays for photonic computation can perform up to 10^{12} multiply-accumulate operations per second.²² Since the light of the same wavelength can propagate simultaneously through different modes in a waveguide, mode-division multiplexing (MDM) technology is now emerging as a powerful tool to further increase the data throughput of PICs.^{23–26} As an example, a multimodulator setup with 4 modes and 4 wavelengths can achieve a data bandwidth of 512 Gbps when operating at 32 Gbps, improving the performance of solely WDM.²⁷ In the field of photonic computing, researchers have begun to apply MDM technology to achieve higher computing speed and density, with initial promising results.^{14,28,29}

To apply MDM, it is necessary to obtain higher-order modes in addition to the fundamental transverse electric mode TE_0 , which can be achieved by an asymmetric directional coupler (DC).^{30,31} Mode conversion can be realized by satisfying phase-matching conditions between TE_0 and higher-order modes.³² In simulations, the mode conversion can be almost lossless, and the degree of conversion can be controlled through asymmetric DC device parameters. However, fabrication errors can affect the conversion between TE_0 and higher-order modes, preventing precise control of the mode conversion.

To mitigate fabrication errors, post-trimming of the fabricated asymmetric DC is expected to control the deviation in mode conversion. Post-trimming has been employed in ring resonators, whereby changing the material refractive index modifies the effective refractive index of TE_0 mode, thereby adjusting the resonance wavelength.^{33–35} Commonly used trimming methods include ultraviolet light³⁶ and electron

Received: April 30, 2024

Revised: July 19, 2024

Accepted: July 22, 2024

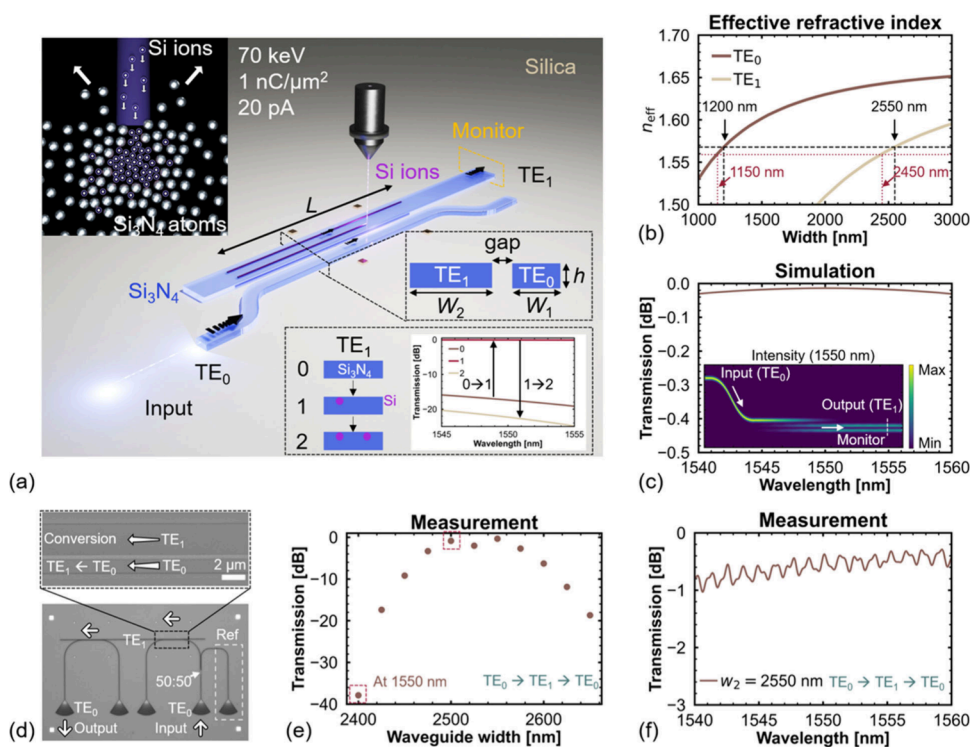


Figure 1. (a) Schematic of the asymmetric DC that converts TE₀ mode to TE₁ mode. The transmission of the asymmetric DC can be trimmed by silicon ion implantation. The inset shows a schematic of the formation of a silicon-rich amorphous region in a Si₃N₄ nanostructure by silicon ion implantation. Implantation energy, dose, and beam current used in silicon ion implantation are also indicated. (b) Effective refractive index of TE₀ and TE₁ modes for different waveguide widths. (c) Simulated transmission spectrum of the asymmetric DC with $w_1 = 1200$ nm, $w_2 = 2550$ nm, gap = 300 nm, and $h = 335$ nm. The n of Si₃N₄ used in the simulation is 2.01. We note that when the n of Si₃N₄ is varied between 1.97 and 2.06 (see SI S2), the insertion loss at 1550 nm remains less than 0.7 dB, which indicates that the mode conversion in the asymmetric DC is insensitive to refractive index changes due to temperature changes (the thermo-optic coefficient of Si₃N₄ is as low as $\sim 2.5 \times 10^{-5}$ K⁻¹).^{42,43} The inset shows the intensity distribution at 1550 nm. (d) Images of the fabricated mode converter. (e) Transmission measurements at 1550 nm for the mode converters with $w_2 = 2400$ to 2650 nm in steps of 25 nm. (f) Measured transmission spectrum of the mode converter with $w_2 = 2550$ nm.

beam irradiation of the cladding chemical resists.^{33,36} However, resist-based trimming cannot guarantee long-term stability because such coatings are affected by light and high temperatures. Ion implantation methods are an attractive alternative, for instance germanium ion implantation,^{37–39} but because germanium absorbs light at 1550 nm, it introduces additional losses into photonic structures (e.g., measured propagation loss is up to 33 dB/mm⁴⁰). In a recent study, silicon ion implantation as a permanent trimming method has shown tremendous performance in tuning the photonic structure without introducing additional losses by virtue of the nature of silicon at telecommunication wavelengths.⁴¹ After annealing, the resonant wavelength of the trimmed ring resonator remained unchanged for 60 days, indicating the excellent long-term stability of silicon ion implantation.⁴¹ Hence, silicon ion implantation appears to provide an excellent platform for trimming asymmetric DCs.

In this study, we propose that the mode conversion of a silicon nitride (Si₃N₄) asymmetric DC can be controlled by silicon ion implantation. By implanting silicon ions on the waveguide, we can vary the transmission of the TE₁ mode by up to 18 dB after mode conversion. In addition, we propose that the effect of trimming on the asymmetric DC depends on the position of the implanted silicon ion on the waveguide, which provides an additional degree of freedom for trimming.

Figure 1a shows a schematic of how mode conversions in an asymmetric DC are trimmed by silicon ion implantation. Silicon ion implantation slightly trims the waveguide, which

changes the properties of the guided mode, resulting in changes in the transmission of the asymmetric DC. Before exploring the effect of silicon ion implantation on the transmission of the asymmetric DCs, we first investigate the TE₀ to TE₁ mode conversion based on asymmetric DCs. As shown in Figure 1a, the asymmetric DC consists of two Si₃N₄ waveguides of widths w_1 and w_2 placed on a silicon dioxide layer (buried oxide layer). In this study, the gap between the two waveguides was set at 300 nm.⁴⁴ The waveguide height h was fixed at 335 nm to avoid the waveguide supporting transverse magnetic modes. In this configuration, light is coupled in and injected from the narrow waveguide in TE₀ mode. To achieve mode conversion, the phase-matching condition must be satisfied, i.e., the effective refractive index of TE₀ mode n_{TE_0} in the narrow waveguide is equal to the effective refractive index of TE₁ mode n_{TE_1} in the wide waveguide. Figure 1b shows the effective refractive indices of the two modes with different waveguide widths. The reason for choosing w_1 to be 1200 nm is that narrower waveguides (e.g., 900 nm) have very high scattering losses in experiments owing to the roughness of waveguide side walls, while wider waveguides (e.g., 1500 nm) require longer coupling lengths of mode conversion due to better field confinement.⁴⁵ After confirming w_1 , w_2 is chosen to be 2550 nm to satisfy the phase-matching condition. The second condition for achieving mode conversion is to choose the appropriate coupling length for the two waveguides. To this end, the optimum coupling length was estimated via simulations (see SI S1) using a 3D simulator

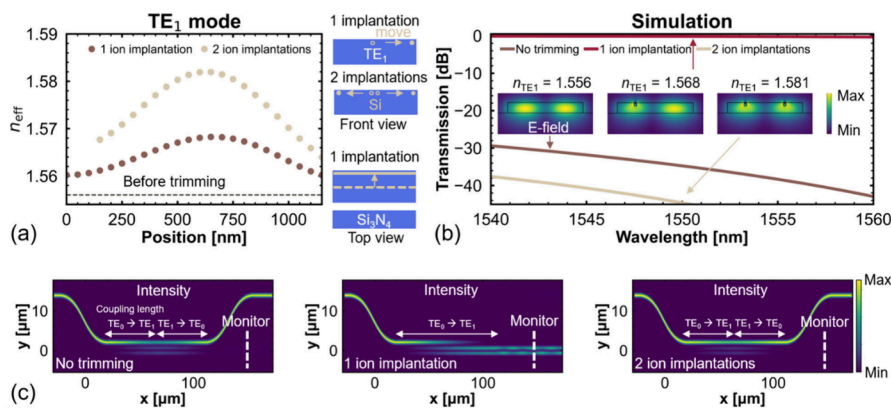


Figure 2. (a) Effective refractive indices of TE₁ mode with respect to position in the waveguide of 2400 nm width before trimming, with one ion implantation, and with two ion implantations. (b) Simulated transmission spectra and (c) intensity distributions at 1550 nm for the asymmetric DC with $w_2 = 2400$ nm before trimming, with one ion implantation, and with two ion implantations. The electric field distribution of the TE₁ mode in the inset is obtained using the Finite-Difference Eigenmode solver from Lumerical, which provides information on the properties of the selected mode, such as electric field distribution and effective refractive index.

(ANSYS Lumerical FDTD) based on the finite-difference time-domain method. The transmission spectrum of the asymmetric DC is shown in Figure 1c. Based on the inset in Figure 1c, we confirm that the input light of the TE₀ mode is fully converted to the light of the TE₁ mode at a coupling length $L = 90$ μm.

Si₃N₄ mode converters were fabricated (see SI S3) to experimentally study the performance of the proposed structure. Figure 1d shows the images of a fabricated mode converter. The input light is coupled to the mode converter through a grating coupler in the form of TE₀ mode. The waveguide width after the grating coupler is 1200 nm and only supports TE₀ mode propagation. A 50:50 multimode interferometer (MMI) is used to split the input light (see SI S4). Half of the input light passes through the first asymmetric DC, is converted to TE₁ mode, and then propagates in the wide bus waveguide. An identical asymmetric DC (the second one) then converts the light from TE₁ mode back to TE₀ mode before the light reaches the output grating coupler. The other half of the input light after the MMI arrives directly at the output grating coupler (white dashed box), and the measurement of this is used as a reference signal for the subsequent normalization process. In this configuration, it can be assumed that the change in the normalized transmission spectrum is due to two mode conversions (TE₀ to TE₁ and back to TE₀). Figure 1e shows the normalized transmission of the mode converters at 1550 nm, with w_2 varying between 2400 to 2650 nm. We observe that the transmission is sensitive to changes in w_2 . When $w_2 = 2400$ nm, the n_{TE_0} is greater than the n_{TE_1} ($n_{\text{TE}_0} > n_{\text{TE}_1}$), resulting in almost zero transmission. As w_2 increases to 2500 nm, the insertion loss decreases to 0.4 dB per asymmetric DC (0.8 dB for two asymmetric DCs). When $w_2 = 2550$ nm, the insertion loss per asymmetric DC is as low as 0.2 dB, meaning that the effective refractive indices of the two modes are nearly matched ($n_{\text{TE}_0} = n_{\text{TE}_1}$). As w_2 increases further, the transmission decreases because $n_{\text{TE}_0} < n_{\text{TE}_1}$.

The transmission spectrum (see SI S5 for the measurement setup) of the mode converter with $w_2 = 2550$ nm is shown in Figure 1f, indicating that the insertion loss per conversion in the experiment can be as low as 0.2 dB. The transmission deviation between 1540 and 1560 nm is only 0.4 dB, indicating that the mode converter operates over a relatively wide wavelength range. However, n_{TE_0} in the narrow waveguides is

more sensitive to width variations than n_{TE_1} in the wide waveguides (Figure 1b: $\Delta n_{\text{TE}_0} > \Delta n_{\text{TE}_1}$), and therefore the performance of the mode converter is degraded by fabrication errors.

To post-trim the mode converters by silicon ion implantation, simulations were performed to theoretically study the effect of silicon ion implantation on the asymmetric DCs of the mode converters. As described later, a silicon-rich region will be formed after silicon ion implantation, but for simplicity, we assume in the simulations that a small region of Si₃N₄ is replaced by pure silicon, as shown in the inset of Figure 2a. The geometry of the replaced region is assumed to be cylindrical with a diameter of ~ 100 nm and a height of 90 μm. The implanted region has a small cross-section and therefore does not support waveguide modes at 1550 nm. Because the refractive index of Si₃N₄ ($n \sim 2$) is smaller than that of silicon ($n \sim 3.47$), the larger the implanted area at a fixed location on the waveguide, the higher the n_{TE_1} . In addition to the cross-sectional area of the implanted region, we propose that the position of the implanted silicon ion on the waveguide is also crucial for the tuning of n_{TE_1} . Moving the implanted region from the center to the edge of the waveguide results in n_{TE_1} fluctuations that first increase and then decrease, with consistent results observed in both directions of movement. This is because the TE₁ mode does not have a uniform electric field distribution in the waveguide, as shown in the inset of Figure 2b. If the implanted region is close to the place where the electric field of TE₁ mode is stronger, the interaction between the implanted silicon region and the TE₁ mode electric field will be stronger and the implantation correspondingly has a greater effect on n_{TE_1} (see SI S6). Similar to the one ion implantation, a similar change in n_{TE_1} occurs when the positions of two ion implantations are moved in opposite directions on the waveguide, as shown in Figure 2a. If the distance from the implantation position to the center of the waveguide is fixed, it can be assumed that two ion implantations further increase n_{TE_1} compared to one ion implantation. The n_{TE_1} curve for the two implantations starts at 150 nm to ensure that the two ion implantations do not overlap spatially.

Figure 2b shows the transmission spectra of the asymmetric DC with $w_1 = 1200$ nm and $w_2 = 2400$ nm. For consistency with the experiments, the transmission spectra are the spectra

after two conversions ($TE_0 \rightarrow TE_1 \rightarrow TE_0$). Here, w_2 decreases from 2550 nm ($n_{TE_0} = n_{TE_1}$) to 2400 nm ($n_{TE_0} > n_{TE_1}$) to introduce a phase mismatch. Due to the phase mismatch between the two modes, the transmission before silicon implantation is close to zero. For the implantation to have a large effect on n_{TE_1} , it is assumed that the center of the implanted region is 625 nm from the center of the waveguide. With one ion implantation, n_{TE_1} increases from 1.556 to 1.568. This small increase in n_{TE_1} can result in a large increase in the transmission from near zero to near unity (see SI S7 for the effect of ion implantation position on the transmission). The second ion implantation further increases n_{TE_1} to 1.581, causing the transmission to return to near zero. We note that the large change in transmission is not only related to the phase matching of the two modes but also to the change in the required coupling length. As shown in Figure 2c, the required coupling length for the asymmetric DCs without trimming or with two ion implantations is almost half of the required coupling length when performing one ion implantation. This means that although the TE_0 mode is partially converted to TE_1 mode, the light of TE_1 mode ends up coupling back to the input waveguide, resulting in negligible transmission at the monitor position. Therefore, it is important to emphasize that silicon ion implantation affects n_{TE_1} and changes in n_{TE_1} affect the coupling length required for mode conversion. Note that although the n of silicon varies slightly with temperature,⁴⁶ this variation has a negligible effect on the mode conversion because the cross-section of the implanted region is much smaller than the cross-section of the waveguide (see SI S2).

Based on the simulation results, we started the experimental study of silicon ion-implanted mode converters. Ion implantation was performed using the Raith VELION focused ion beam (FIB) device (see SI S8). Figures 3a and 3b show a schematic of silicon ion implantation. To better understand the effect of silicon ion implantation on the waveguides, scanning transmission electron microscope (STEM) energy-dispersive spectroscopy (EDS) analysis was employed to study the cross-section of the cut waveguide (see SI S9). Figures 3c and 3d show the STEM EDS elemental mapping of the implanted waveguide and the corresponding line scan profile depicted by the dashed line area on the cross-section of the implanted region. In the STEM EDS micrographs, brighter regions indicate a localized increase in the fraction of specific atoms and darker regions indicate a decrease in the fraction of specific atoms. An increase in the fraction of silicon atoms and a decrease in the fraction of nitrogen atoms is observed in the implanted region. Note that as a light element, the fraction of nitrogen may be slightly overestimated (see SI S10).⁴⁷ The corresponding elemental line scan profile further confirms the increase of silicon in the implanted region, indicating the formation of a silicon-rich amorphous region inside the Si_3N_4 waveguide after bombardment by incident ions. It should be noted that the cross-sectional shape (e.g., circular or elliptical) and position (e.g., depth of the implantation area) of the implanted region have a negligible effect on the trimming performance as long as n_{TE_1} is the same after trimming (see SI S7 and S11).

Figure 4a shows a scanning electron microscope (SEM) micrograph of the mode converter with $w_2 = 2400$ nm after performing two ion implantations. Figure 4b shows the transmission spectra of the mode converter with $w_2 = 2400$ nm before trimming (brown curve), after the first ion implantation (red curve), and after the second ion

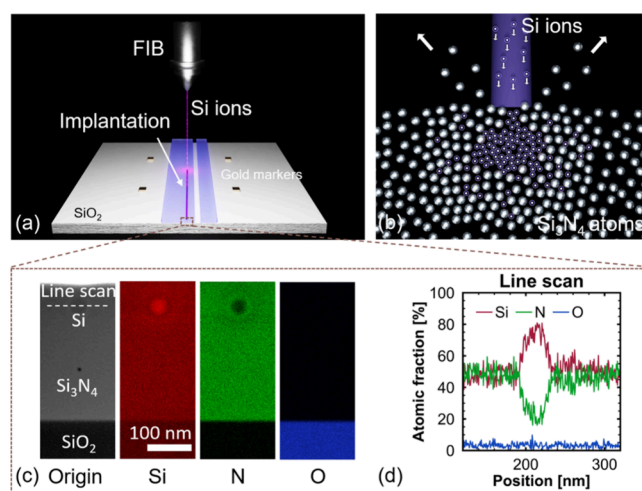


Figure 3. (a) Schematic of silicon ion implantation on a Si_3N_4 waveguide. (b) Schematic of the mechanism of the silicon ion implantation process. Upon reaching the Si_3N_4 waveguide, the high-energy silicon ions, accelerated to 70 keV, initiate surface sputtering and collision cascades that result in the ejection of atoms into the air or their displacement from their original position. This process, in conjunction with the creation of vacancies and alterations in the free volume of amorphous Si_3N_4 , supports the ongoing diffusion and buildup of incoming silicon ions within the waveguide, ultimately resulting in the formation of a silicon-rich amorphous region inside the Si_3N_4 . (c) The STEM EDS elemental mapping of the waveguide and (d) the line scan profile that provide precise spatial distributions of each element in the implanted region.

implantation (cream curve). Due to the phase mismatch ($n_{TE_0} > n_{TE_1}$), the transmitted light is barely measured for the original mode converter. The reason for the almost no light could easily be misinterpreted as the phase mismatch completely inhibits the coupling between the two modes. However, as mentioned earlier (see Figure 2c), a small phase mismatch does not completely suppress the mode conversion. According to our previous simulation results, another reason for the decrease in the transmission is the change in the required coupling length. Compared to 90 μm for the ideal model ($w_1 = 1200$ nm and $w_2 = 2550$ nm), the required coupling length of the asymmetric DC with $w_2 = 2400$ nm is almost halved (~ 50 μm). This means that if the length of the coupling region remains unchanged at 90 μm , the light is again reverse-coupled to the input waveguide. After the first ion implantation, an increase of 18 dB in transmission per asymmetric DC is observed (36 dB in total). Losses due to silicon ion implantation are negligible (see SI S12), so we believe that the insertion loss here is related to the coupling length (see SI S13). After the second ion implantation, the transmission is again reduced to close to zero. The transmission is suppressed for the same reason as in the mode converter before trimming. Subsequently, we perform a simulation study of the measured spectra of the mode converter with $w_2 = 2400$ nm. For simplicity, we assume that the shape of the implanted region is cylindrical and ignore any gradients for elements near the boundary of the implanted region. As shown in Figure 4c, the simulation results are in good agreement with the measurements, and the simulated field distributions are similar to those in Figure 2c, which supports our interpretation of the experimental results for the mode converter with $w_2 = 2400$ nm in this paragraph.

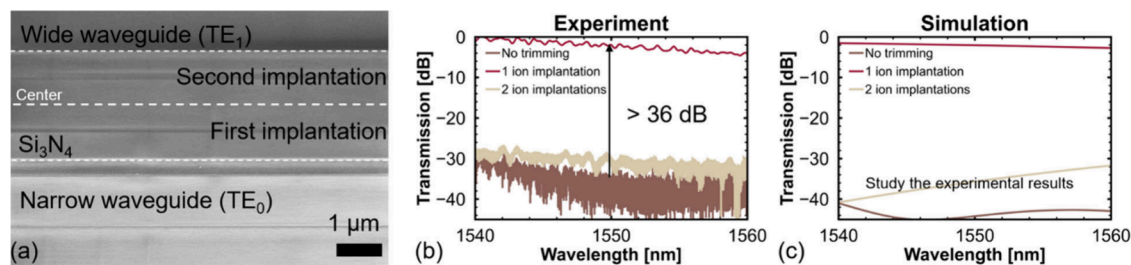


Figure 4. (a) A SEM micrograph of the asymmetric DC with $w_2 = 2400$ nm after two silicon ion implantations. (b) Measured and (c) simulated spectra of the mode converter with $w_2 = 2400$ nm before trimming, with one ion implantation, and with two ion implantations.

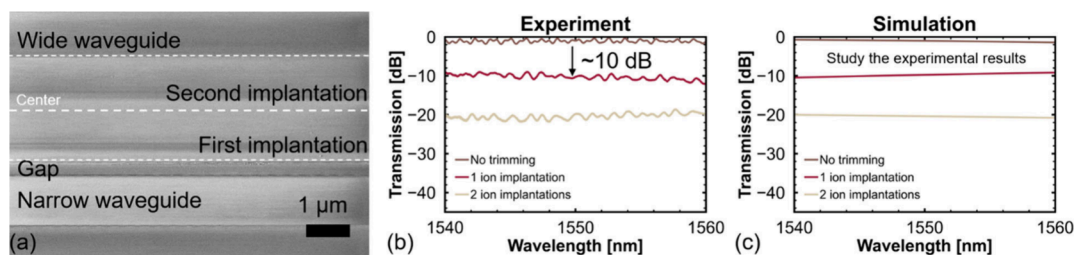


Figure 5. (a) A SEM micrograph of the asymmetric DC with $w_2 = 2500$ nm after two ion implantations. (b) Measured and (c) simulated spectra of the mode converter with $w_2 = 2500$ nm before trimming, with one ion implantation, and with two ion implantations.

The magnitude of the asymmetric DC transmission change can be controlled by changing the position of the ion implantation on the waveguides (see SI S14). Figure 5a shows a micrograph of the asymmetric DC with $w_2 = 2500$ nm. Compared to the implantation positions of the asymmetric DCs with $w_2 = 2400$ nm, the implantation positions are deviated (~ 250 nm) from the position where they have the greatest effect on n_{TE1} , and therefore have less effect on n_{TE1} , resulting in a smaller change in the transmission of the asymmetric DC, as shown in Figure 5b. The influence of the one ion implantation on the asymmetric DC transmission variation is reduced from 18 to 5 dB. The simulation results in Figure 5c are in good agreement with the measurement results.

In summary, we present an asymmetric DC-based Si_3N_4 mode converter and propose that the mode conversion between TE_0 and TE_1 modes can be controlled by silicon ion implantation. The insertion loss per asymmetric DC of this mode converter is as low as 0.2 dB. We observe that the performance of the mode converters is very sensitive to the variation of the waveguide width due to fabrication errors, which can be mitigated by post-trimming. Post-trimming of the fabricated mode converters via silicon ion implantation is demonstrated successfully and is used to locally change the waveguide material, thereby effectively tuning n_{TE1} . The trimmed mode converter can achieve transmission changes of as high as 18 dB per asymmetric DC. In addition, the variation of the mode converter's transmission is related to the position of the ion implantation on the waveguide. By precisely controlling the position of the implanted silicon ion, we achieve a 5-dB transmission change per asymmetric DC. This study provides a method for tuning n_{TE1} to enable control of the mode converters, advancing the development of higher-order mode photonic structures. This development paves the way for multimode photonic accelerators in neuromorphic computing.

■ ASSOCIATED CONTENT

Supporting Information

The Supporting Information is available free of charge at <https://pubs.acs.org/doi/10.1021/acs.nanolett.4c02065>.

1. The models used in the FDTD simulations; 2. Temperature-dependent response of asymmetric DCs before and after silicon ion implantation; 3. The sample fabrication procedure; 4. The multimode interferometer used in the study; 5. The measurement device for the transmission spectra; 6. The effect of silicon ion implantation on the electric field distribution of the TE_1 mode; 7. Variation of the asymmetric DC transmission with different ion implantation positions; 8. Process in performing silicon ion implantation; 9. Techniques for microscopic analysis and related sample preparation; 10. Discussion of the microscopic analysis results after silicon ion implantation; 11. Influence of cross-sectional shapes of silicon ion implanted region; 12. Loss introduced by silicon ion implantation is negligible; 13. Cause of insertion loss in trimmed asymmetric DCs; 14. Overview of the control of transmission variations by changing the silicon ion implantation position (PDF)

■ AUTHOR INFORMATION

Corresponding Author

Wolfram H. P. Pernice – Kirchhoff-Institute for Physics, Heidelberg University, 69120 Heidelberg, Germany; orcid.org/0000-0003-4569-4213; Email: wolfram.pernice@kip.uni-heidelberg.de

Authors

Rongyang Xu – Kirchhoff-Institute for Physics, Heidelberg University, 69120 Heidelberg, Germany; orcid.org/0000-0001-8914-4454

Shabnam Taheriniya – Kirchhoff-Institute for Physics, Heidelberg University, 69120 Heidelberg, Germany

Akhil Varri – Institute of Physics, University of Münster, 48149 Münster, Germany
Mark Ulanov – Kirchhoff-Institute for Physics, Heidelberg University, 69120 Heidelberg, Germany
Iurii Konyshev – Kirchhoff-Institute for Physics, Heidelberg University, 69120 Heidelberg, Germany
Linus Krämer – Kirchhoff-Institute for Physics, Heidelberg University, 69120 Heidelberg, Germany
Liam McRae – Kirchhoff-Institute for Physics, Heidelberg University, 69120 Heidelberg, Germany
Falk Leonard Ebert – Kirchhoff-Institute for Physics, Heidelberg University, 69120 Heidelberg, Germany
Julian Rasmus Bankwitz – Kirchhoff-Institute for Physics, Heidelberg University, 69120 Heidelberg, Germany
Xinyu Ma – Kirchhoff-Institute for Physics, Heidelberg University, 69120 Heidelberg, Germany
Simone Ferrari – Kirchhoff-Institute for Physics, Heidelberg University, 69120 Heidelberg, Germany
Harish Bhaskaran – Department of Materials, University of Oxford, Oxford, Oxfordshire OX1 3PH, U.K.; orcid.org/0000-0003-0774-8110

Complete contact information is available at:
<https://pubs.acs.org/10.1021/acs.nanolett.4c02065>

Author Contributions

¹R.X. and S.T. contributed equally to this work

Notes

The authors declare no competing financial interest.

ACKNOWLEDGMENTS

R.X. gratefully acknowledges the Alexander-von-Humboldt Foundation for providing a postdoctoral fellowship. W.H.P.P. acknowledges support from the Deutsche Forschungsgemeinschaft (DFG, German Research Foundation) under project numbers 390761711 and 390900948. The work was also supported by the European Union's EXCELLENT SCIENCE - Future and Emerging Technologies (FET) (PHOENICS, grant no. 101017237) and The European Innovation Council (EIC) (HYBRAIN, grant no. 101046878). The manuscript was written through the contributions of all authors. All authors have approved the final version of the manuscript.

REFERENCES

(1) Dai, D.; Wang, J.; Shi, Y. Silicon Mode (de)Multiplexer Enabling High Capacity Photonic Networks-on-Chip with a Single-Wavelength-Carrier Light. *Opt. Lett.* **2013**, *38* (9), 1422.
(2) Hsu, Y.; Chuang, C.-Y.; Wu, X.; Chen, G.-H.; Hsu, C.-W.; Chang, Y.-C.; Chow, C.-W.; Chen, J.; Lai, Y.-C.; Yeh, C.-H.; Tsang, H. K. 2.6 Tbit/s On-Chip Optical Interconnect Supporting Mode-Division-Multiplexing and PAM-4 Signal. *IEEE Photon. Technol. Lett.* **2018**, *30* (11), 1052–1055.
(3) Wu, X.; Huang, C.; Xu, K.; Zhou, W.; Shu, C.; Tsang, H. K. 3 × 104 Gb/s Single-λ Interconnect of Mode-Division Multiplexed Network With a Multicore Fiber. *J. Lightwave Technol.* **2018**, *36* (2), 318–324.
(4) Elshaari, A. W.; Pernice, W.; Srinivasan, K.; Benson, O.; Zwiller, V. Hybrid Integrated Quantum Photonic Circuits. *Nat. Photonics* **2020**, *14* (5), 285–298.
(5) Khasminkaya, S.; Pyatkov, F.; Slowik, K.; Ferrari, S.; Kahl, O.; Kovalyuk, V.; Rath, P.; Vetter, A.; Hennrich, F.; Kappes, M. M.; Gol'tsman, G.; Korneev, A.; Rockstuhl, C.; Krupke, R.; Pernice, W. H. P. Fully Integrated Quantum Photonic Circuit with an Electrically Driven Light Source. *Nature Photon* **2016**, *10* (11), 727–732.

(6) Lenzini, F.; Gruhler, N.; Walter, N.; Pernice, W. H. P. Diamond as a Platform for Integrated Quantum Photonics. *Adv. Quantum Tech* **2018**, *1* (3), 1800061.

(7) He, X.; Htoon, H.; Doorn, S. K.; Pernice, W. H. P.; Pyatkov, F.; Krupke, R.; Jeantet, A.; Chassagneux, Y.; Voisin, C. Carbon Nanotubes as Emerging Quantum-Light Sources. *Nat. Mater.* **2018**, *17* (8), 663–670.

(8) Wang, J.; Sciarrino, F.; Laing, A.; Thompson, M. G. Integrated Photonic Quantum Technologies. *Nat. Photonics* **2020**, *14* (5), 273–284.

(9) Bogaerts, W.; Pérez, D.; Capmany, J.; Miller, D. A. B.; Poon, J.; Englund, D.; Morichetti, F.; Melloni, A. Programmable Photonic Circuits. *Nature* **2020**, *586* (7828), 207–216.

(10) Xu, R.; Taheriniya, S.; Ovyvan, A. P.; Bankwitz, J. R.; McRae, L.; Jung, E.; Brücknerhoff-Plückelmann, F.; Bente, I.; Lenzini, F.; Bhaskaran, H.; Pernice, W. H. P. Hybrid Photonic Integrated Circuits for Neuromorphic Computing [Invited]. *Opt. Mater. Express* **2023**, *13* (12), 3553–3606.

(11) Brücknerhoff-Plückelmann, F.; Feldmann, J.; Gehring, H.; Zhou, W.; Wright, C. D.; Bhaskaran, H.; Pernice, W. Broadband Photonic Tensor Core with Integrated Ultra-Low Crosstalk Wavelength Multiplexers. *Nanophotonics* **2022**, *11* (17), 4063–4072.

(12) Huang, Y.; Yue, H.; Ma, W.; Zhang, Y.; Xiao, Y.; Tang, Y.; Tang, H.; Chu, T. Parallel Photonic Acceleration Processor for Matrix-Matrix Multiplication. *Opt. Lett.* **2023**, *48* (12), 3231.

(13) Cheng, Z.; Ríos, C.; Pernice, W. H. P.; Wright, C. D.; Bhaskaran, H. On-Chip Photonic Synapse. *Sci. Adv.* **2017**, *3* (9), No. e1700160.

(14) Bai, Y.; Xu, X.; Tan, M.; Sun, Y.; Li, Y.; Wu, J.; Morandotti, R.; Mitchell, A.; Xu, K.; Moss, D. J. Photonic Multiplexing Techniques for Neuromorphic Computing. *Nanophotonics* **2023**, *12* (5), 795–817.

(15) Chakraborty, I.; Saha, G.; Roy, K. Photonic In-Memory Computing Primitive for Spiking Neural Networks Using Phase-Change Materials. *Phys. Rev. Applied* **2019**, *11* (1), 014063.

(16) Meng, X.; Zhang, G.; Shi, N.; Li, G.; Azaña, J.; Capmany, J.; Yao, J.; Shen, Y.; Li, W.; Zhu, N.; Li, M. Compact Optical Convolution Processing Unit Based on Multimode Interference. *Nat. Commun.* **2023**, *14* (1), 3000.

(17) Shen, Y.; Harris, N. C.; Skirlo, S.; Prabhu, M.; Baehr-Jones, T.; Hochberg, M.; Sun, X.; Zhao, S.; Larochelle, H.; Englund, D.; Soljačić, M. Deep Learning with Coherent Nanophotonic Circuits. *Nature Photon* **2017**, *11* (7), 441–446.

(18) Yang, L.; Ji, R.; Zhang, L.; Ding, J.; Xu, Q. On-Chip CMOS-Compatible Optical Signal Processor. *Opt. Express* **2012**, *20* (12), 13560–13565.

(19) Dong, P. Silicon Photonic Integrated Circuits for Wavelength-Division Multiplexing Applications. *IEEE J. Select. Topics Quantum Electron.* **2016**, *22* (6), 370–378.

(20) Liu, Ansheng; Liao, Ling; Chetrit, Y.; Basak, J.; Nguyen, H.; Rubin, D.; Paniccia, M. Wavelength-Division Multiplexing Based Photonic Integrated Circuits on Silicon-on-Insulator Platform. *IEEE J. Select. Topics Quantum Electron.* **2010**, *16* (1), 23–32.

(21) Chen, L.; Doerr, C. R.; Dong, P.; Chen, Y. Monolithic Silicon Chip with 10 Modulator Channels at 25 Gbps and 100-GHz Spacing. *Opt. Express* **2011**, *19* (26), B946–B951.

(22) Feldmann, J.; Youngblood, N.; Karpov, M.; Gehring, H.; Li, X.; Stappers, M.; Le Gallo, M.; Fu, X.; Lukashchuk, A.; Raja, A. S.; Liu, J.; Wright, C. D.; Sebastian, A.; Kippenberg, T. J.; Pernice, W. H. P.; Bhaskaran, H. Parallel Convolutional Processing Using an Integrated Photonic Tensor Core. *Nature* **2021**, *589* (7840), 52–58.

(23) Luo, L.-W.; Ophir, N.; Chen, C. P.; Gabrielli, L. H.; Poitras, C. B.; Bergmen, K.; Lipson, M. WDM-Compatible Mode-Division Multiplexing on a Silicon Chip. *Nat. Commun.* **2014**, *5* (1), 3069.

(24) Chen, G.; Yu, Y.; Zhang, X. Monolithically Mode Division Multiplexing Photonic Integrated Circuit for Large-Capacity Optical Interconnection. *Opt. Lett.* **2016**, *41* (15), 3543.

- (25) Gostimirovic, D.; Ye, W. N. Compact Silicon-Photonic Mode-Division (de)Multiplexer Using Waveguide-Wrapped Microdisk Resonators. *Opt. Lett.* **2021**, *46* (2), 388.
- (26) Liu, Y.; Xu, K.; Wang, S.; Shen, W.; Xie, H.; Wang, Y.; Xiao, S.; Yao, Y.; Du, J.; He, Z.; Song, Q. Arbitrarily Routed Mode-Division Multiplexed Photonic Circuits for Dense Integration. *Nat. Commun.* **2019**, *10* (1), 3263.
- (27) Jia, H.; Zhang, L.; Ding, J.; Zheng, L.; Yuan, C.; Yang, L. Microring Modulator Matrix Integrated with Mode Multiplexer and De-Multiplexer for on-Chip Optical Interconnect. *Opt. Express* **2017**, *25* (1), 422–430.
- (28) Yin, R.; Xiao, H.; Jiang, Y.; Han, X.; Zhang, P.; Chen, L.; Zhou, X.; Yuan, M.; Ren, G.; Mitchell, A.; Tian, Y. Integrated WDM-Compatible Optical Mode Division Multiplexing Neural Network Accelerator. *Optica* **2023**, *10* (12), 1709–1718.
- (29) Wu, C.; Yu, H.; Lee, S.; Peng, R.; Takeuchi, I.; Li, M. Programmable Phase-Change Metasurfaces on Waveguides for Multimode Photonic Convolutional Neural Network. *Nat. Commun.* **2021**, *12* (1), 96.
- (30) Zhang, Z.; Hu, X.; Wang, J. On-Chip Optical Mode Exchange Using Tapered Directional Coupler. *Sci. Rep.* **2015**, *5* (1), 16072.
- (31) Dai, D.; Wang, S. Asymmetric Directional Couplers Based on Silicon Nanophotonic Waveguides and Applications. *Front. Optoelectron.* **2016**, *9* (3), 450–465.
- (32) Shu, H.; Shen, B.; Deng, Q.; Jin, M.; Wang, X.; Zhou, Z. A Design Guideline for Mode (DE) Multiplexer Based on Integrated Tapered Asymmetric Directional Coupler. *IEEE Photonics J.* **2019**, *11* (5), 1–12.
- (33) Thiel, L.; Logan, A. D.; Chakravarthi, S.; Shree, S.; Hestroffer, K.; Hatami, F.; Fu, K.-M. C. Precise Electron Beam-Based Target-Wavelength Trimming for Frequency Conversion in Integrated Photonic Resonators. *Opt. Express* **2022**, *30* (5), 6921.
- (34) Prorok, S.; Petrov, A. Yu.; Eich, M.; Luo, J.; Jen, A. K.-Y. Trimming of High-Q-Factor Silicon Ring Resonators by Electron Beam Bleaching. *Opt. Lett.* **2012**, *37* (15), 3114.
- (35) Biryukova, V.; Sharp, G. J.; Klitis, C.; Sorel, M. Trimming of Silicon-on-Insulator Ring-Resonators via Localized Laser Annealing. *Opt. Express* **2020**, *28* (8), 11156.
- (36) Farmakidis, N.; Yu, H.; Lee, J. S.; Feldmann, J.; Wang, M.; He, Y.; Aggarwal, S.; Dong, B.; Pernice, W. H. P.; Bhaskaran, H. Scalable High-Precision Trimming of Photonic Resonances by Polymer Exposure to Energetic Beams. *Nano Lett.* **2023**, *23* (11), 4800–4806.
- (37) Jayatilaka, H.; Frish, H.; Kumar, R.; Heck, J.; Ma, C.; Sakib, M.; Huang, D.; Rong, H. Post-Fabrication Trimming of Silicon Photonic Ring Resonators at Wafer-Scale. *J. Lightwave Technol.* **2021**, *39* (15), 5083–5088.
- (38) Yu, X.; Chen, X.; Milosevic, M. M.; Shen, W.; Topley, R.; Chen, B.; Yan, X.; Cao, W.; Thomson, D. J.; Saito, S.; Peacock, A. C.; Muskens, O. L.; Reed, G. T. Ge Ion Implanted Photonic Devices and Annealing for Emerging Applications. *Micromachines* **2022**, *13* (2), 291.
- (39) Milosevic, M. M.; Chen, X.; Cao, W.; Runge, A. F. J.; Franz, Y.; Littlejohns, C. G.; Mailis, S.; Peacock, A. C.; Thomson, D. J.; Reed, G. T. Ion Implantation in Silicon for Trimming the Operating Wavelength of Ring Resonators. *IEEE J. Select. Topics Quantum Electron.* **2018**, *24* (4), 1–7.
- (40) Chen, X.; Milosevic, M. M.; Runge, A. F. J.; Yu, X.; Khokhar, A. Z.; Mailis, S.; Thomson, D. J.; Peacock, A. C.; Saito, S.; Reed, G. T. Silicon Erasable Waveguides and Directional Couplers by Germanium Ion Implantation for Configurable Photonic Circuits. *Opt. Express* **2020**, *28* (12), 17630.
- (41) Varri, A.; Taheriniya, S.; Brückerhoff-Plückelmann, F.; Bente, I.; Farmakidis, N.; Bernhardt, D.; Rösner, H.; Kruth, M.; Nadzeyka, A.; Richter, T.; Wright, C. D.; Bhaskaran, H.; Wilde, G.; Pernice, W. H. P. Scalable Non-Volatile Tuning of Photonic Computational Memories by Automated Silicon Ion Implantation. *Adv. Mater.* **2024**, *36*, 2310596.
- (42) Johnson, K.; Alshamrani, N.; Almutairi, D.; Grieco, A.; Horvath, C.; Westwood-Bachman, J. N.; McKinlay, A.; Fainman, Y. Determination of the Nonlinear Thermo-Optic Coefficient of Silicon Nitride and Oxide Using an Effective Index Method. *Opt. Express* **2022**, *30* (26), 46134.
- (43) Arbabi, A.; Goddard, L. L. Measurements of the Refractive Indices and Thermo-Optic Coefficients of Si₃N₄ and SiO_x Using Microring Resonances. *Opt. Lett.* **2013**, *38* (19), 3878.
- (44) Li, D.; Li, B.; Tang, B.; Zhang, P.; Yang, Y.; Liu, R.; Xie, L.; Li, Z. Broadband Silicon Nitride Power Splitter Based on Bent Directional Couplers with Low Thermal Sensitivity. *Micromachines* **2022**, *13* (4), 559.
- (45) Xu, Dan-Xia; Schmid, J. H.; Reed, G. T.; Mashanovich, G. Z.; Thomson, D. J.; Nedeljkovic, M.; Chen, Xia; Van Thourhout, D.; Keyvaninia, S.; Selvaraja, S. K. Silicon Photonic Integration Platform—Have We Found the Sweet Spot? *IEEE J. Select. Topics Quantum Electron.* **2014**, *20* (4), 189–205.
- (46) Li, H. H. Refractive Index of Silicon and Germanium and Its Wavelength and Temperature Derivatives. *J. Phys. Chem. Ref. Data* **1980**, *9* (3), 561–658.
- (47) *Transmission Electron Microscopy*; Carter, C. B.; Williams, D. B., Eds.; Springer International Publishing: Cham, 2016. DOI: 10.1007/978-3-319-26651-0.